The role of dissolved rice husk ash in the development of binary blast furnace slag-sewage sludge ash alkali-activated mortars

Danilo Bordan Istuque[a], *Jordi Payá*[b], *Lourdes Soriano*[b], *Maria Victoria Borrachero*[b], *José Monzó*[b], *Mauro Mitsuuchi Tashima*[a*]

[a] Universidade Estadual Paulista (UNESP), Faculdade de Engenharia de Ilha Solteira, MAC – Grupo de Pesquisa em Materiais Alternativos de Construção, Ilha Solteira, SP, Brazil.

[b] ICITECH – Instituto de Ciencia y Tecnología del Hormigón, Universitat Politècnica de València (UPV), Valencia, Spain.

*Corresponding author: maumitta@hotmail.com

Abstract

This study evaluated the compressive strength performance and microstructure of binary blast furnace slag-sewage sludge ash (BFS-SSA) alkali-activated mortars, in which rice husk ash (RHA) was dissolved in NaOH to replace commercial sodium silicate. The dissolution of RHA, performed in a thermal bottle with NaOH solution, enhanced the compressive strength of the alkali-activated mortars based on BFS up to 4.5-fold. BFS-SSA based mortars (10-40% SSA), activated with NaOH/RHA-based sodium silicate suspensions, reached a compressive strength up to 30 MPa after 28 curing days at 20ºC. The RHA dissolution enhanced the strength and sustainability of the BFS-SSA alkali-activated mortars.

Keywords: Alkaline activation, Rice husk ash, Sodium silicate suspensions, Sewage sludge ash, Blast furnace slag, Microstructure

Highlights

- Blast furnace slag (BFS) and sewage sludge ash (SSA) mixtures were used as precursors
- The strength of BFS-SSA alkali-activated mortars is enhanced using NaOH/RHA-based sodium silicate suspensions
- Compressive strength above 30 MPa was achieved for the BFS-SSA alkali-activated mortars
- The main gel formation in the BFS-SSA alkali-activated materials was C-(N)-A-S-H
- SSA increased the occurrence of porous C-(N)-A-S-H gel type

1. Introduction.

Attention to alkali-activated materials (AAMs) is spreading worldwide, mainly due to environmental issues like waste management and carbon footprint reduction. AAMs are mostly produced by alkali-activation of calcium-aluminosilicate by-products or wastes from agriculture and industry [1–3], being branded as a low carbon footprint alternative to Portland cement according to life cycle assessment (LCA) studies [4–6]. However, some studies have warned that the carbon footprint of AAMs strongly depends on factors such as type and quantity of alkaline activators used (NaOH and Na_2SiO_3, for example) for their production. The CO_2 emission rates of AAMs reported in the literature are divergent but are in line with the attribution of the activator that most contributes to the carbon footprint of AAMs to Na_2SiO_3[4,7]. Therefore, reducing the carbon footprint of activators is the most representative challenge faced by AAMs production [8,9], exceeding the necessity of searching for alternative precursors.

Interesting AAMs that have been recently studied are produced with sewage sludge ash (SSA), which is from sewage sludge incineration in wastewater treatment plants [10], and blast furnace slag (BFS). According to the Ecoinvent Life Cycle Inventory database, the environmental emission factor for BFS (as a by-product) is estimated at 19.2 $kgCO_2eq/t$ [7], considering only its secondary production, which includes solidification (granulated BFS) and grinding (BFS). For SSA, no CO_2 emissions are attributed, except for its conditioning pre-treatment and transport emissions, which can vary depending on their employment. Therefore, BFS and SSA are interesting raw materials for AMMs production, and the sustainability enhancement of this kind of AMMs should be of common interest.

Tashima et al. [11] reported a study on BFS-SSA alkali-activated mortars using NaOH as the activator. The best results were obtained for mortars with 20 wt.% of SSA and 80 wt.% of BFS, activated with an optimized solution of 6 $mol.kg^{-1}$ NaOH, whose compressive strength at 90 curing days and 20°C was 31 MPa. Chakraborty et al. [12] combined SSA (70 wt.%), quicklime (20 wt.%) and BFS (10 wt.%), using NaOH as an alkaline activator, to achieve a maximum compressive strength of 31.3 MPa for 28 curing days at room temperature. However, in this case, a higher NaOH aqueous solution concentration (12 $mol.kg^{-1}$) was required to prepare this system with a high SSA content, which gave a less sustainable binder. Chen et al. [13] evaluated the compressive strength and microstructure of AAMs containing 50 wt.% of SSA and 50 wt.% of BFS (water/precursor ratio of 0.2, dry-mixed method). However, to achieve good compressive strength, a mixed alkaline solution composed of NaOH and Na_2SiO_3 was required. These authors pointed out that the SiO_2/Na_2O molar ratio was a significant factor in developing the compressive strength for the BFS-SSA alkali-activated material. The highest compressive strength (32.8 MPa; 28 curing days at room temperature) was optimized for a Na_2O content and SiO_2/Na_2O molar ratio of 4% and 0.95, respectively

[13]. Nevertheless, as previously presented, sodium silicate use implied a higher carbon footprint for these AAMs type. Therefore, to obtain good mechanical development and better sustainability for this system type, which is an important alternative for managing SSA, a more environmental-friendly sodium silicate source is required apart from low NaOH consumption.

As reported in the literature, an alternative silica source to produce sodium silicate activators is rice husk ash (RHA) [14,15]. RHA is a residue obtained from incinerating rice husk to produce energy, and it is a type of residue that is largely generated worldwide [16]. For example, the world rice crop production in 2018/19 was 496.5 million tonnes, which could estimate the generation of approximately 25.0 million tonnes of RHA in one year [17]. Many studies have pointed out the effectiveness of RHA dissolution in alkaline solution (NaOH or KOH solution). Hydrothermal methods, or even simple methods as mixing the materials with water at room temperature, can be used to produce a sodium silicate suspension, by means of RHA dissolution, as a substitute for the commercial reagent [14,16–20]. RHA dissolution is optimized with the thermal processes depending on the time and temperature of treatment [14,21], inclusively dissolving the crystalline silica, apart from the amorphous silica content, as pointed out by Mejía et al. [15] that evaluated the dissolution of RHA composed of high crystalline phases content as cristobalite and quartz. However, those thermal processes could increase the energy consumption required to produce the AAMs, which is not suitable for a more sustainable AMMs development. A notable method found in literature, used to solubilize the silica from sugarcane straw ash, is a thermal-bottle method, that harnesses energy released from the NaOH dissolution to improve the silica dissolution [22]. This is a thermal method with less energy consumption that could also be applied to solubilize the silica from RHA.

Although RHA has been used as a silica source for obtaining more environmentally friendly alkaline activators [19] for AMMs production, the mechanical performance of BFS-SSA based AAMs prepared with this kind of alkaline activator has never been evaluated. Hence, the novelty of the current study is related to using non-conventional sodium silicate activators made with NaOH and RHA, which apart from being more sustainable than using commercial Na_2SiO_3, could offer significant compressive strength improvement for BFS-SSA alkali-activated mortars, reaching higher performance than one displayed when used NaOH activators. Such strength enhancement might assure high SSA incorporation content in alkali-activated mortars with satisfactory mechanical performance. Therefore, the present study aims to evaluate the compressive strength and microstructural development of the BFS-SSA alkali-activated mortars, in which RHA is previously dissolved with NaOH using the thermal-bottle method. By considering this goal, compressive strength tests, mercury intrusion porosimetry (MIP), thermogravimetry (TGA/DTG), X-ray diffraction (XRD), X-ray fluorescence (XRF), and field emission scanning electron microscopy (FESEM) studies were performed to characterise the raw materials and BFS-SSA alkali-activated pastes or mortars.

2. Material and methods.

2.1. Materials.

BFS was supplied by the Cementval company (Puerto de Sagunto, Valencia, Spain) and used as a precursor to produce AAMs. In the Speedy model ball mill of Nannetti, BFS was ground (BFS/ball mass ratio of 0.36, 2 cm diameter balls, 30-minute grinding). SSA, used as precursor replacement of BFS, was collected in the Pinedo wastewater treatment plant (Valencia, Spain) from the electrostatic precipitator in the fluidised bed incinerator. The Dacsa company (Tabernes Blanques, Spain) supplied RHA, which was ground in an industrial mill. Sodium silicate suspensions (sodium silicate + undissolved RHA) were prepared with RHA and NaOH pellets (98% purity). Siliceous sand was used to prepare mortars.

2.2. Methods.

Firstly, physicochemical characterisation of the raw materials was carried out (see Section 2.2.1). Secondly, the influence of the NaOH concentration of the alkaline activator was analysed on the BFS alkali-activated mortars, in which RHA was added in two different ways (see Section 2.2.2). Thirdly, the influence of BFS replacement with SSA on the mechanical strength of binary (BFS-SSA) alkali-activated mortars was assessed (see Section 2.2.3). The mortars in sections 2.2.2 and 2.2.3 were mechanically evaluated by means of compressive strength tests (see Section 2.2.4). Finally, physicochemical characterisation was conducted on pastes and mortars according to the findings in the previous steps (see Section 2.2.5).

2.2.1. Physicochemical characterisation of raw materials

All raw materials (BFS, SSA and RHA) were characterised by means of Malvern Mastersizer 2000 laser granulometer in water suspension, Philips MagiX Pro Spectrometer (X-ray fluorescence, XRF), Bruker AXS D8 Advanced diffractometer (X-ray diffraction, XRD), where was used a current intensity of 20 mA at 40 kV, a step angle of 0.02º, a step time of 2.0 s/step with Cu-Kα radiation, and a Ni filter within the 5–70º range), and finally by means of ZEISS Supra 55 microscopy (field emission scanning electron microscopy, FESEM) using carbon to coat samples. An extractive treatment method with hydrochloric acid and 4 M KOH, for an optimized extraction time treatment of 3 min, was applied to distinguish between the reactive silica and insoluble residue [23] of RHA.

2.2.2. Production of BFS alkali-activated mortars with addition of RHA.

The mix proportions of alkali-activated mortars are presented in Table 1. The NaOH concentration of the activator was 4 or 8 mol.kg^{-1}. Samples A0-m and D0-m were produced as reference mortars, which were prepared by mixing BFS, sand and NaOH solution. The inclusion of RHA, carried out in addition to binder mass (BFS), was performed in two different ways: a) as solid RHA mixed with BFS (samples B0-m and C0-m); b) as dissolved RHA (samples PB0-m, PC0-m and PD0-m), following the method used to produce sodium silicate suspensions described by Moraes et al. [22]. The heat released from the NaOH dissolution inside a thermal bottle improves the silica dissolution present in RHA. Adding RHA in a sufficient content gave an equivalent theoretical SiO_2/Na_2O molar ratio (ε) to 1.5 or 3 when considering both crystalline and amorphous silica phases which could dissolve during the dissolution of RHA [15]. The sodium silicate suspensions were prepared 24 h before mortars were produced. The insoluble content from the RHA dissolution was maintained in the suspension. The water/binder (w/b) ratio and the sand/binder (s/b) mass ratio of the mortars was set at 0.5 and 3, respectively, and the BFS mass was the binder. Mixing mortar proceeding was: 30 sec for sodium silicate suspensions stirring; 30 sec for adding the binder; 120 min mixing the paste; 30 sec for adding sand; and 60 min mixing the final mixture. Fresh mortars were cast into a prismatic mould of 40 × 40 × 160 mm^3 and vibrated for 100 sec. Moulds were sealed with low-density polyethylene (LDPE) plastic film to avoid excessive water loss during curing. The alkali-activated mortars were cured in a thermal bath at 65ºC, being demoulded after 4 h, and remained sealed with LDPE plastic film in the thermal bath until compressive strength testing.

Table 1. Mix proportion of the BFS alkali-activated mortars

Identification	NaOH [mol.kg^{-1}]	ε#	water/binder	sand/binder	BFS (binder, wt.%)	Addition of RHA (wt.% vs. BFS)
A0-m	4	--	0.5	3	100	0
B0-m		1.5				*10
PB0-m						**10
C0-m		3.0				*20
PC0-m						**20
D0-m	8	--				0
PD0-m		0.7				**10

ε: theoretical SiO_2/Na_2O molar ratio. RHA was added as (*) solid RHA and as (**) dissolved RHA.

2.2.3. Production of the binary BFS-SSA alkali-activated mortars.

In order to assess the effect of SSA, and to achieve its maximum incorporation by replacing BFS (maintaining the same amount of water), different solid BFS-SSA mixtures were prepared by considering

the dose that displayed better mechanical performance from the study carried out in the previous step: this dose was taken as the reference. The limit replacement of BFS by SSA was set by the critical workability to the casting of the mortars (with a fixed amount of water) using a vibration table. The w/b ratio and the s/b ratio were set at 0.5 and 3, respectively. In this step, the binder was the sum of BFS and SSA. The mixing mortar proceeding was the same previously reported in item 2.2.2. Fresh mortars were also cast in a prismatic mould (40 × 40 × 160 mm^3) that was vibrated for 100 s. After sealing with LDPE film, samples were cured in a thermal bath at 65ºC or in a moist room (>95%) at 20ºC. They were demoulded after 4 h when cured at 65ºC or after 24 h when cured at 20ºC. All the samples remained sealed with LDPE plastic film in these environments until the compressive strength tests.

2.2.4. Compressive strength test.

The mechanical performance of mortars was evaluated by means of compressive strength according to UNE 196-1:2018 [24] by means of Universal Machine Ibertest (model MEH-3000-LCMD2W, 3000 kN). The compressive strength for each mortar was the average of at least five values. The compressive strength test ages of mortars were 3 and/or 7 days when cured at 65ºC, and 7, 28 and 91 days when cured at 20ºC.

2.2.5. Physicochemical characterization of alkali-activated pastes or mortars

Thermogravimetry analysis (TG/DTG), XRD, and field emission scanning electron microscopy with energy dispersive X-ray spectroscopy (FESEM-EDX) were carried out for the characterisations of the pastes, and mercury intrusion porosimetry (MIP) were carried out for characterisations of both pastes and mortars. For XRD and TG/DTG analyses, at each curing age, the pastes were jointly grinding with acetone in an agate mortar to stop the reactions, filtered and then dried during 30 min in an oven at 65°C. These analyses were carried out on the sieved solid part with particle diameter under 125 μm. For FESEM-EDX analyses, fractured surfaces of the pastes were obtained and immersed at acetone for 1 h, to stop the reactions, being afterwards dried in an oven at 65°C for 30 min. For MIP analyses, at the test age, undamaged mortar and paste fragments with approximately 1 cm^3 were immersed into acetone for 24 h to stop the reactions and then dried for 2 h in an oven at 65°C. The XRD diffractograms were obtained as mentioned in item 2.2.1. The TGA curves were acquired at a temperature range of 35-600ºC, where the sample was heated in a sealed-pinholed aluminium crucible at a heating rate of 10ºC.min^{-1} in an N_2 atmosphere (75 mL.min^{-1} gas flow) by means of a Mettler Toledo TGA850 thermobalance. The FESEM micrographs of the fractured surface pastes were taken using a ZEISS Supra 55. Carbon was used to coat samples. For EDX analyses of small areas were applied an extra high tension of 20 kV and a 6–8 mm working distance, while to capture

the FESEM micrographs were applied tension of 2 kV and a 4-6 mm working distance. The pore distribution in the MIP tests (range of 91.2-5.5 nm, the equivalent to pressures between 2 psia and 32989 psia) was measured by an Autopore IV 9500 from Micromeritics Instrument Corporation.

3. Results and Discussion.

3.1. Physicochemical characterisation of the raw materials

BFS was ground to obtain a mean particle diameter of 30.4 µm, with d(0.1), d(0.5) and d(0.9) being 1.8 µm, 20.9 µm and 73.0 µm, respectively. The mean particle diameter of SSA was 30.5 µm, with d(0.1), d(0.5) and d(0.9) being 3.0 µm, 25.9 µm and 65.4 µm, respectively. The mean particle diameter of RHA was 20.3 µm, with d(0.1), d(0.5) and d(0.9) being 2.5 µm, 10.5 µm and 41.3 µm, respectively. The chemical compositions of BFS, SSA and RHA are summarised in Table 2. Both BFS and SSA are mainly composed of SiO_2, CaO and Al_2O_3, in agreement with the literature [10,25]. The XRD analyses of BFS and SSA are shown in Fig. 1. Although SSA is composed of crystalline phases, such as quartz, anhydrite, lime, portlandite, hydroxylapatite, albite and forsterite, a diffuse hump within the 24-36° 2θ range showed that a small part of SSA was amorphous. In the XRD diffractogram of BFS, a remarkable diffuse hump within the 20-40° 2θ range was seen, which is characteristic of this slag [26]. Besides the crystalline peaks of quartz in BFS, calcite was also identified, which is likely due to the carbonation that occurred while storing the slag [27]. The presence of calcite in BFS composition could justify the unusual high loss on ignition (LOI) of 5.53%, apart from possibly a little moisture. The morphology of particles for each raw material (BFS, SSA and RHA) is observed in Fig. 2. All the materials presented irregular particle shapes, and SSA was also composed of some rounded particles. Furthermore, SSA particles are porous with notable roughness, which could significantly affect the water absorption in binders [28]. Although RHA presented a rich silica content (85.58%), the amorphous RHA content was calculated to be 31.5%, a similar value to the one (27%) report by Mejía et al., that evaluated the dissolution of RHA with high crystalline content [15]. According to the XRD pattern of RHA, such a crystalline part is composed of mineral phases as quartz, tridymite and cristobalite.

Table 2. Chemical composition of precursors (BFS and SSA) and RHA.

	Oxide composition (%)											
Material	***SiO_2***	***CaO***	***Al_2O_3***	***Fe_2O_3***	***Na_2O***	***MgO***	***K_2O***	***P_2O_5***	***SO_3***	***Cl***	***Others***	***LOI***
BFS	30.53	40.15	10.55	1.29	0.87	7.43	0.57	0.26	1.93	0.06	0.83	5.53
SSA	26.43	31.96	10.39	7.66	0.40	2.63	2.00	5.92	8.57	0.13	1.7	2.20
RHA	85.58	1.83	0.25	0.21	-	0.50	3.39	0.67	0.26	0.32	-	6.99

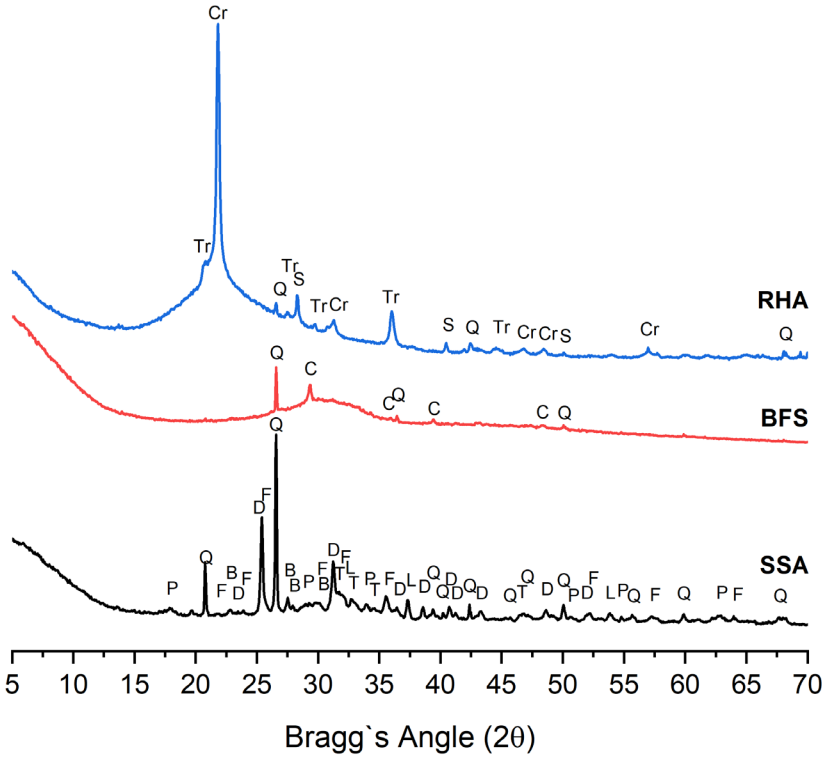

Fig. 1. XRD diffractogram of precursor materials (BFS and SSA). Q - quartz (SiO_2, PDFcard 331161), D - anhydrite ($CaSO_4$, PDFcard 371496), L - lime (CaO, PDFcard 371497), P - portlandite ($Ca(OH)_2$, PDFcard 040733), H - hydroxylapatite ($Ca_5(PO_4)_3(OH)$, PDFcard 090432), B - albite ($NaAlSi_3O_8$, PDFcard 200572), F - forsterite (Mg_2SiO_4, PDFcard 340187), C - calcite ($CaCO_3$, PDFcard 050586), Tr – trydimite (SiO_2, PDFcard 181170), Cr – cristobalite (SiO_2, PDFcard 391425), and S – silvine (KCl, PDFcard 411476).

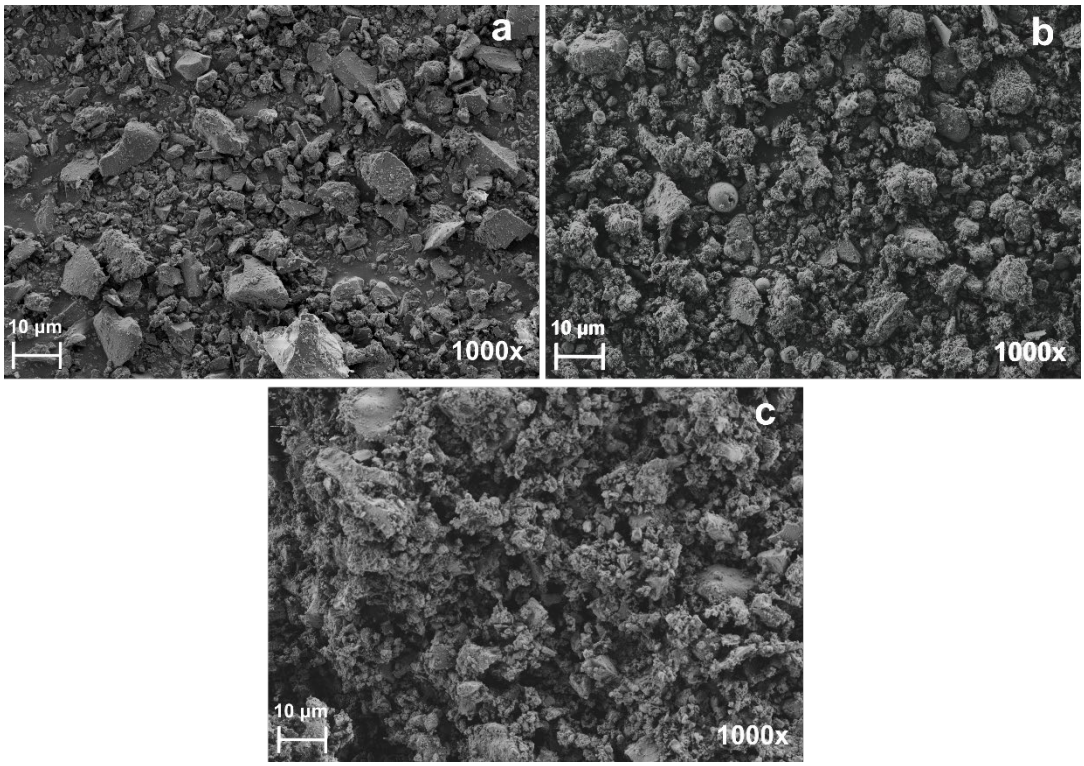

Fig. 2. FESEM micrographs of BFS (a), SSA (b) and RHA (c).

3.2. Compressive strength of the BFS alkali-activated mortars with RHA addition.

The compressive strength values of the reference alkali-activated mortars (NaOH as the activating reagent, A0-m for 4 mol.kg^{-1} NaOH and D0-m for 8 mol.kg^{-1} NaOH) and the alkali-activated mortars containing RHA (B0-m, PB0-m, C0-m, PD0-m) are depicted in Fig. 3. No significant difference in compressive strength (14% improvement when increasing from 4 to 8 mol.kg^{-1}) appeared for the reference mortars at different NaOH concentrations. Both reference mortars A0-m and D0-m developed low compressive strength, with 11.4 and 13.0 MPa, respectively, after 7 curing days at 65ºC. These values implied that the NaOH concentration of 4 mol.kg^{-1} was the better option bearing in mind that it involved less alkali consumption, which led to a more environmentally friendly binder [4]. Tashima et al. [11] reported a higher compressive strength of 24.6 MPa for BFS-based mortars (for 28 curing days at 25°C, sand/BFS mass ratio of 2.5, w/b of 0.45) activated with NaOH aqueous solution of 6 mol.kg^{-1}, which corroborates that superior compressive strength performance cannot be obtained with high NaOH concentration, taking into account that a compressive strength loss occurred when increasing the NaOH concentration from 6 to 10 mol.kg^{-1}.

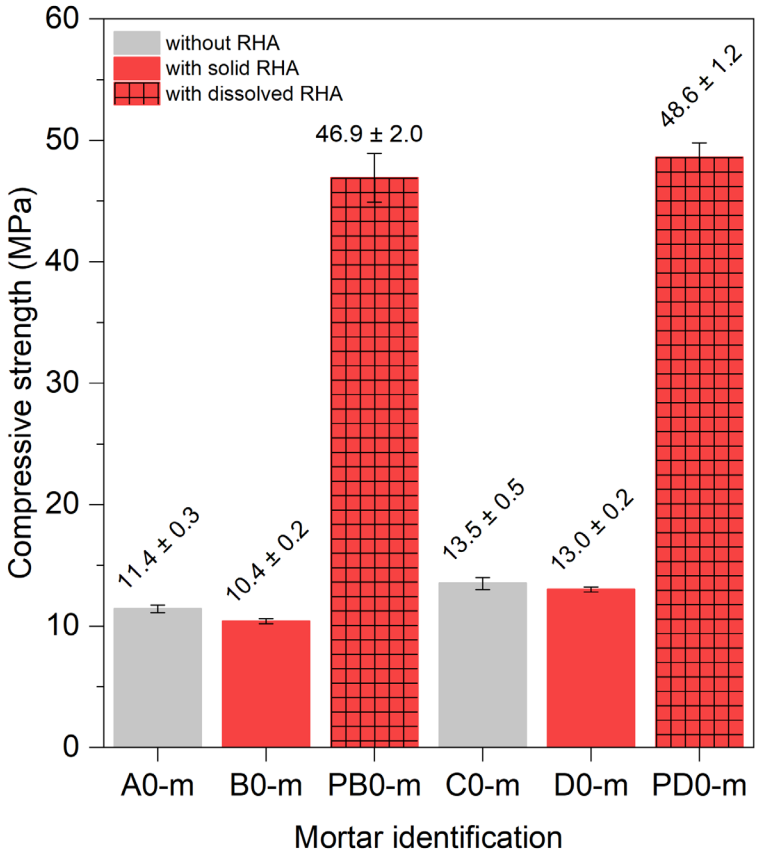

Fig. 3. Compressive strength of BFS alkali-activated mortars, cured for 7 days at 65ºC, without the addition of RHA and with the addition of solid RHA or dissolved RHA.

The comparison made between the compressive strength values of mortars A0-m and B0-m revealed that adding RHA with no previous dissolution had no significant influence on compressive strength of mortars. Furthermore, when doubling the amount of solid RHA in the mortar C0-m mix, compressive strength increased only by 3.1 MPa (from 10.4 to 13.5 MPa). This slight increase (29.8%) in compressive strength was hard to distinguish and it could have been due to a physical or chemical effect of RHA, or to both.

Mortars PB0-m and PC0-m were produced in the same mix proportion as those proposed for mortars B0-m and C0-m, but in this case, RHA was previously dissolved in a thermal bottle with NaOH solution (4 $mol.kg^{-1}$ of NaOH and ε of 1.5) for 24 h, in which part of the silica from RHA was dissolved as sodium silicate [21]. The formulated sodium silicate suspension contributed significantly to developing the compressive strength of mortar PB0-m. The compressive strength of this mortar (46.9 MPa) was approximately 4.5-fold superior to that of mortar B0-m (10.4 MPa). The RHA dissolution increased silicate availability at the start of the reaction, improving the precipitation of silicate-containing hydrates products, which led to greater

compressive strength [14,18,20]. With an equivalent mortar to C0-m, for which a higher dissolved RHA addition content was used (ε=3), mortar workability problems occurred due to the higher viscosity of the alkaline suspension (PC0-m in Table 1). As the amount of RHA increased when preparing the sodium silicate suspension, the viscosity of the final suspension was probably higher due to both the effect of water absorption by the undissolved RHA particles and the silicate concentration [29]. So, it was not possible to cast this mortar.

In order to verify whether a higher NaOH concentration would improve RHA dissolution and, consequently, silicate concentration in the alkaline suspension, mortar PD0-m was produced using the same mix proportion as that employed for mortar PB0-m, but dissolving RHA in a solution with 8 mol.kg^{-1} NaOH (ε=0.7). The comparison between the compressive strength of mortars PB0-m and PD0-m showed that the rise in the NaOH concentration from 4 to 8 mol.kg^{-1} did not considerably improve compressive strength development. Both mortars PB0-m and PD0-m obtained similar compressive strength values, 46.9 and 48.6 MPa, respectively. Although temperature can affect the dissolution rate of RHA in alkaline medium [14], and as the initial temperature during the reaction of RHA depended on the heat released from the NaOH dissolution [22], using 8 mol.kg^{-1} did not offer better results. According to Tong et al. [14], the dissolution of RHA could reach a maximum with 2-3 M NaOH, but this also depends on temperature and dissolution time.

3.3. Compressive strength of the binary BFS-SSA alkali-activated mortars.

In line with the study carried out on the BFS-based systems, sample PB0-m, which was prepared with the previous dissolution of RHA in a solution with 4 mol.kg^{-1} of NaOH (ε=1.5), was established as a standard mix proportion to carry out developing binary BFS-SSA alkali-activated mortars. The maximum replacement of BFS with SSA, for a workability limit to cast mortars using a vibration table, was 40 wt.%, by maintaining the same amount of water as in the mix proportion. Thus, mortars with 10 wt.% (PB10-m), 20 wt.% (PB20-m), 30 wt.% (PB30-m) and 40 wt.% (PB40-m) were produced. The compressive strengths of these mortars cured in a thermal bath (65ºC; 3 and 7 days) and at room temperature (20ºC; 7, 28 and 90 days) are depicted in the Fig. 4.

The compressive strength data were adjusted by a linear fit model, where adjustment parameter R^2 of the equations was 0.95 and 0.98 at 3 and 7 curing days, respectively, for the mortars cured at 65ºC, and was 0.98 at 7 and 28 days, and 0.85 at 91 days for the mortars cured at 20ºC. As the amount of SSA increased, a proportionally decreasing trend of compressive strength was noticed for both curing conditions. Compressive strength generally decreased in proportion and came close to the percentage of the replaced

BFS. However, according to the slope of the linear adjustment equations, SSA negatively affected compressive strength development for longer curing ages; that is, the fitted lines of the compressive strength at 7 days/65ºC and 91 days/20ºC had higher slope values (in absolute values) than those for early curing ages. When the compressive strength values obtained from the linear regression equations of the mortars cured at 65ºC (see in Fig. 4) and at 20°C (see in Fig. 4b) were employed, the relative compressive strength gain (CSG) [30] was calculated and is depicted in Fig. 5. The CSG quantifies the compressive strength supplied by replacing the original binder (BFS as the precursor in this case) by a tested material (SSA in this case), and by comparing to the hypothetical behaviour of the mortar made by replacing the binder with an inert material at the same proportion. Generally, as the percentage of the SSA increased, the CSG also increased. However, it was noted that SSA supplied more significant CSG values for the mortars cured at 65ºC, which could be attributed to the effect of temperature on the reactivity of the mineral admixtures [31]. For the mortars cured at 20ºC, it was noted that the CSG was only substantial at the 28-day curing age compared to those cured at 65ºC. Despite the slight reactive behaviour highlighted by the CSG, it is important to consider that SSA can also play a significant role as a filler [32,33]. Even though the replacement of BFS with SSA resulted in lower compressive strength, SSA did not affect the alkaline activation of the remaining BFS using the sodium silicate suspension produced with RHA. Even with the highest SSA contents (30% and 40%), the mortars developed compressive strengths that came close to 30 MPa. In addition, the curing of the BFS-SSA alkali-activated mortars at 20ºC was an excellent condition to produce mortars as compressive strength performance came close to (at 28 days), or was even superior (at 90 days), then those cured at 65ºC for 7 days. Furthermore, curing at room temperature leads to a more environmentally friendly alkali-activated mortar as it uses less energy than thermal-bath curing.

In order to verify if a higher NaOH concentration would increase the compressive strength of the binary systems, a test was run by preparing a mortar with a similar mix proportion to mortar PD0-m (Table 1), but by replacing 30 wt.% of BFS with SSA, which was cured for 7 days at 65ºC. When increasing the NaOH concentration (to 8 $mol.kg^{-1}$), compressive strength dropped to 28.7±1.9 MPa: the comparison to the binary system sample with the same proportion of SSA (30%) and under the same curing condition, but prepared with 4 $mol.kg^{-1}$ NaOH (PB30-m, which reached 34.7 MPa after 7 days at 65ºC, see Fig. 4), showed that the increase in NaOH did not offer any advantage. Thus, a lower NaOH concentration in the binary BFS-SSA mortars led to better performance and a more sustainable alternative.

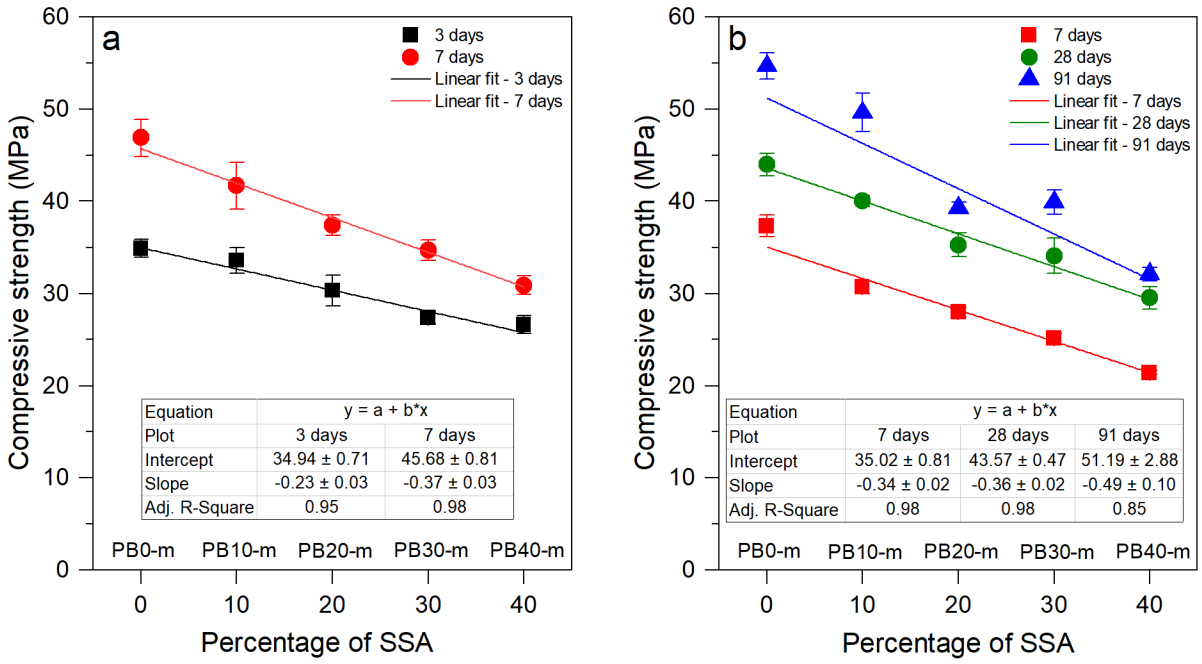

Fig. 4. Compressive strengths of the binary BFS-SSA alkali-activated mortars cured in a thermal bath at 65ºC (a) and room temperature (20°C) (b).

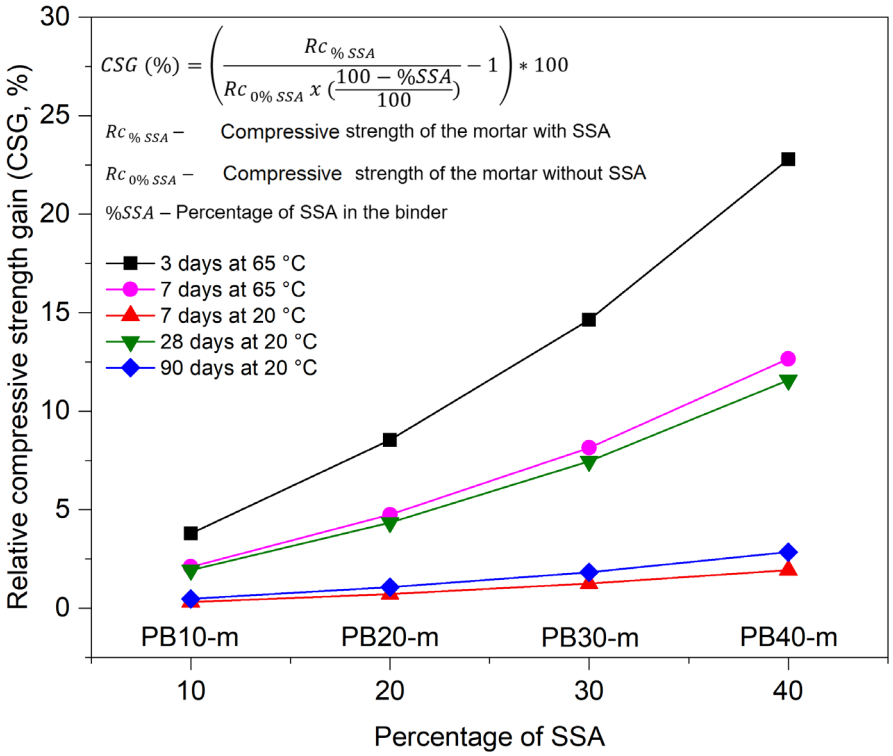

Fig. 5. Relative Compressive Strength Gain (CSG) supplied by SSA in the binary BFS-SSA alkali-activated mortars. The compressive strength values for each curing condition (65ºC or 20ºC) and each curing time (t) were calculated by taking into account the fitting equations listed in Fig. 4.

Comparing the compressive strength of the mortar with the highest SSA content (PB40-m) with the literature results, which present different BFS-SSA alkali-activated systems, it was found that this SSA content was 2-fold higher than that reported by Tashima et al. [11] by, for instance, reaching the same compressive strength level. Although comparing the compressive strengths of pastes and mortars is not suitable, Chen et al. [13] also reached the same compressive strength level by following a dry-mixed process to produce BFS-SSA alkali-activated pastes at the 1:1 proportion. However, they used commercial sodium silicate solutions, which resulted in a less environmentally friendly contribution given the carbon footprint attributed to sodium silicate [34]. Furthermore, the dry-mixed process required an external compressive force to compact samples, which differentiates the application of this material compared to a fluid one. Even though Chakraborty et al. [12] developed a ternary system containing SSA (70 wt.%), quicklime (20 wt.%) and BFS (10 wt.%), to reach the same compressive strength of approximately 30 MPa, a large amount of NaOH was required, which was 3-fold more than that the amount used in the present study. Therefore, the binary BFS-SSA system, prepared with sodium silicate suspension obtained by RHA dissolution in NaOH

solution, proved an outstanding alternative to incorporate large amounts of SSA (40 wt.%), maintained satisfactory compressive strength (~30 MPa), reduced the carbon footprint by removing the commercial sodium silicate and used less NaOH [7].

3.4. Microstructural characterisation of the binary BFS-SSA alkali-activated systems.

3.4.1. Thermogravimetry analyses.

Thermogravimetry analyses were carried out with the binary BFS-SSA alkali-activated pastes, for two different SSA contents (10 and 40 wt.% SSA), identified as PB10-p and PB40-p (equivalents to mortars PB10-m and PB40-m, respectively). Furthermore, a thermogravimetry analysis was also conducted on pastes BFS (B0-p and PB0-p), the equivalents to mortars B0-m and PB0-m, taken as the reference samples, respectively. The TG curves of the pastes cured at 65ºC (7 days) and 20ºC (7 and 28 days) are depicted in Fig. 6, and the total mass of those ones are summarised in Table 3. The derivative thermogravimetric curves (DTG) of the pastes cured at 65ºC (7 days) and 20ºC (7 and 28 days) are represented in Fig. 7 and Fig. 8, respectively. Regardless of temperature and curing ages, the major mass loss occurred between 100ºC and 300ºC in all the samples. Therefore, the minor mass loss within the range from 100ºC to 140ºC (R1 zone) could be attributed to release physico-chemical bonded water, which came from the structure of the C-S-H and/or C-(N)-S-H gel types. However, the most important gel formation was of the C-A-S-H and/or C-(N)-A-S-H type, with dehydration within the range from 140ºC to 300ºC (R2 zone) [20,22]. This agrees with the literature, which reports that the main reaction products formed in the high-calcium AAMs were C-S-H, C-(x)-S-H, C-A-S-H and C-(x)-A-S-H, where x would be Na^+ incorporated as part of the gel to neutralise the gel structure charge [26,35]. Furthermore, due to the significant MgO content in the BFS chemical composition (7.43%, see Table1), hydrotalcite is commonly formed as a product of the BFS-based AAMs [36]. In the DTG curves, a slight mass loss peak appears around 400°C, which could be attributed to the decomposition of the hydrotalcite [37]. In addition, a slight mass loss in the range 250-300°C was noted, although an overlapping mass loss of some products in the R_2 region, likely due to a katoite dehydroxylation [37], mainly in the pastes without SSA.

The comparison of the DTG curves and the total mass loss between samples B0-p and PB0-p, both cured at 65ºC for 7 days, clearly showed the effect of dissolved RHA. In this case, the total mass loss (Table 3 and Fig. 6) of samples B0-p and PB0-p was 7.5% and 12.8%, respectively. Therefore, the sodium silicate suspension, produced by RHA dissolution in NaOH, enhanced the gel formation of the BFS alkali-activation. This result agrees with compressive strength development, which markedly increased when RHA was previously dissolved. The replacement of BFS with SSA decreased the total mass loss up to

approximately 30% in the samples with 40% SSA for the longest curing age, independently of curing temperature. This difference also agrees with the compressive strength of the mortar whose compressive strength reduced close to the replacement percentage of BFS with SSA.

Comparing the DTG curves of samples PB0-p and PB40-p, both cured at 65ºC for 7 days, it was observed a displacement of the main peak from 153ºC to 163ºC. This displacement of the main mass loss peak would likely mean that the replacement of BFS with SSA changed the stoichiometry of the reaction products: the proportion between the mass loss values related to the formed products, according to those observed for zones R1 and R2, substantially changed. The same behaviour was also observed for the samples cured at 20ºC, for which the DTG temperature peak changed from 161ºC (PB0-p) to 163ºC (PB40-p), and from 143ºC (PB0-p) to 153ºC (PB40-p) at 7 and 28 days, respectively. Although SSA and BFS presented similar SiO_2, Al_2O_3 and CaO contents, SSA is composed of some crystalline phases containing mainly Si and Ca, which could imply a change in the reactions due to a lower reactivity of these phases.

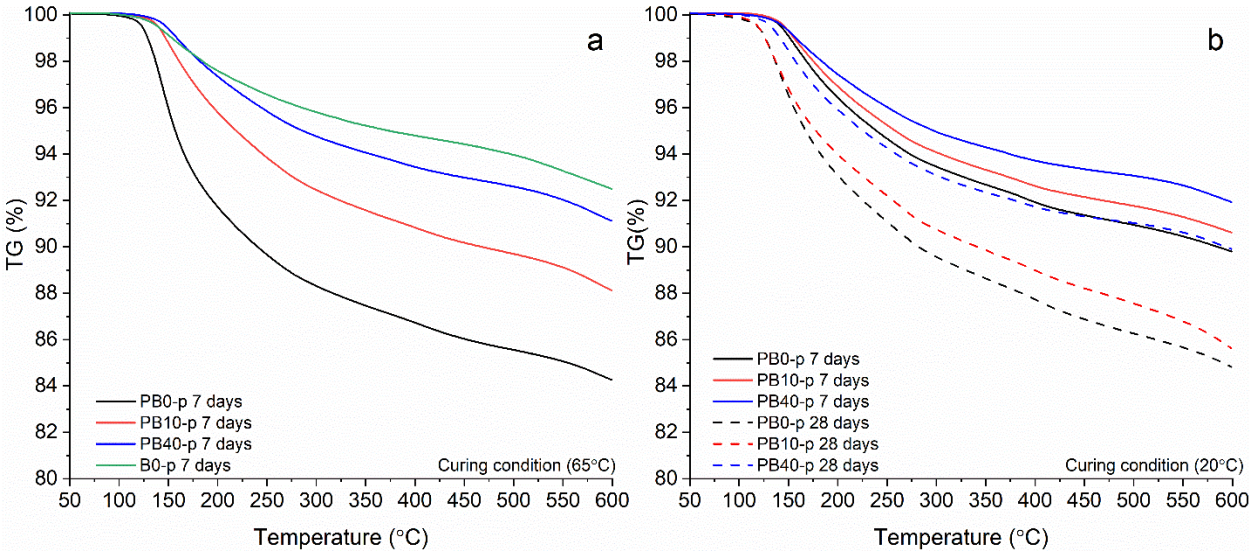

Fig. 6. TG curves of the binary BFS-SSA alkali-activated pastes cured at 65ºC for 7 days (a), and cured at 20°C for 7 days and 28 days (b).

Table 3. Total mass loss of the alkali-activated pastes in the thermogravimetric analysis.

		Total weight loss (%)		
		65°C	20°C	
Identification	**SSA (wt.%)**	**7 days**	**7 days**	**28 days**
B0-p	0	7.5	-	-
PB0-p	0	12.8	10.2	15.2
PB10-p	10	11.9	9.4	14.4

PB40-p	40	8.9	8.1	10.1

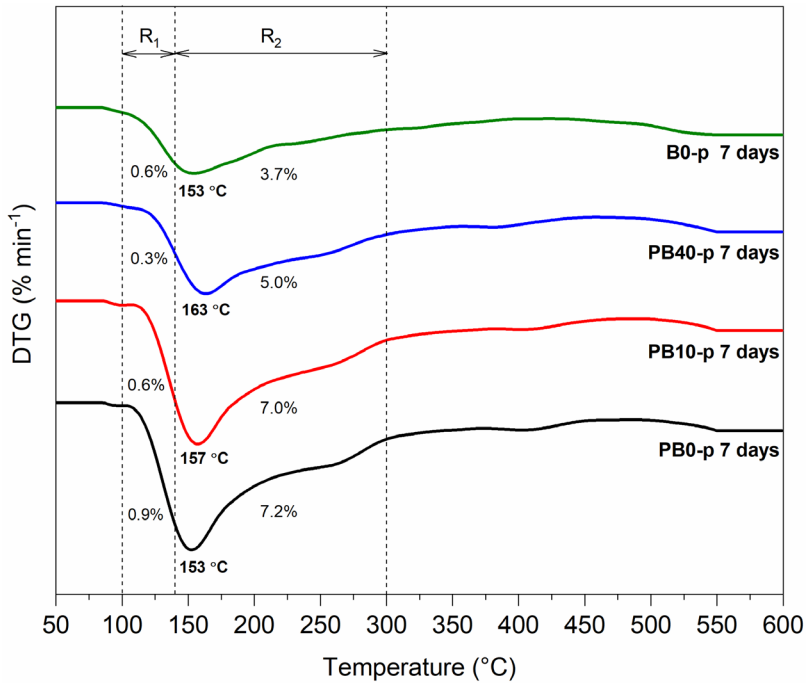

Fig. 7. DTG curves of the binary BFS-SSA alkali-activated pastes cured at 65ºC for 7 days.

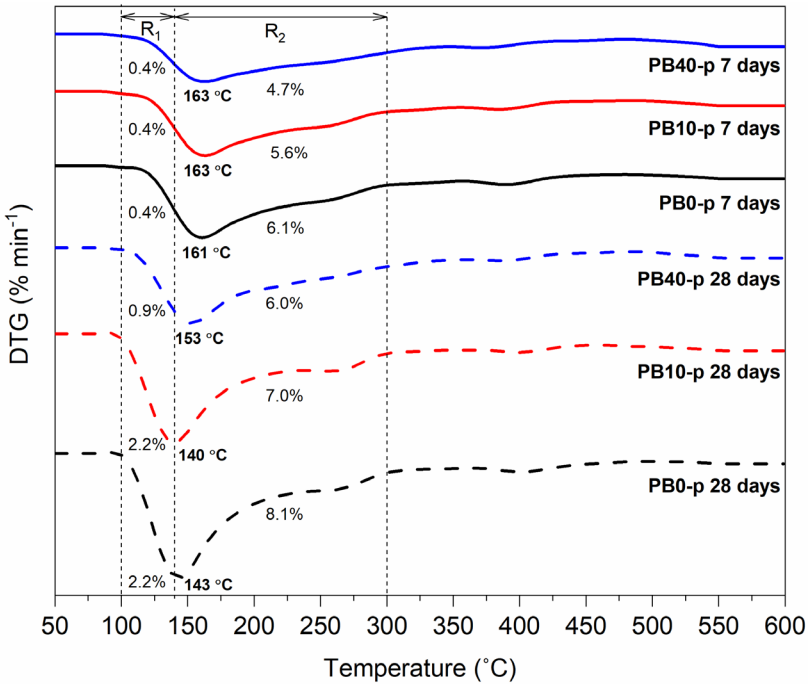

Fig. 8. DTG curves of the binary BFS-SSA alkali-activated pastes cured at 20ºC for 7 and 28 days.

3.4.2. X-ray diffraction analyses.

The XRD diffractogram of the paste samples without SSA (PB0-p) and with 40% SSA (PB40-p) cured for 7 days at 65ºC and for 28 days at 20ºC are shown in Fig. 9. All the samples presented a broad hump within the 20° - 40° range of Bragg`s angle, which is attributed to gel formation due to alkaline activation [13,38]. In accordance with the literature, the main peaks identified in the alkali-activation of BFS (PB0-p) are phases such as calcite, hydrotalcite, katoite and albite [26,39,40]. As BFS was replaced with SSA, both the availability of MgO and Al_2O_3 and the Al_2O_3/Na_2O ratio changed, which affected the occurrence of hydrotalcite and katoite. The intensity of the characteristic peaks of the hydrotalcite-like phase in samples PB40-p was less marked than in samples PB0-p. Furthermore, no katoite peaks were detected in the XRD diffractogram of sample PB40-p, agreeing with the DTG analyses. According to the study carried out by Bae et al. [37], lowering the MgO content led to less content in the hydrotalcite-like phases, and katoite formation only occurred at a proper Al_2O_3/Na_2O ratio of 1. Besides, katoite formation lowers the potential occurrence of zeolite phases [37], which can be associated with the formation of natrolite-zeolite type in paste PB40-p. The natrolite formation could be favoured by a greater relative Na_2O availability for BFS activation if taking into account that the 40% BFS replacing was been conducted by a material (SSA) with lower reactivity [41]. Particularly in the sample PB0-p, cured at 65ºC, grossular was formed, which is expected to occur at a high curing temperature [42,43]. The calcite peaks in all the pastes were due to calcite being present in the original BFS [44]. Quartz peaks appeared in the XRD diffractogram of the samples containing SSA, which was attributed to the unreacted particles of SSA [10]. Besides, other crystalline phases, such as forsterite and albite, were also identified in the diffractograms of the pastes with SSA, which demonstrated the presence of unreacted particles of SSA.

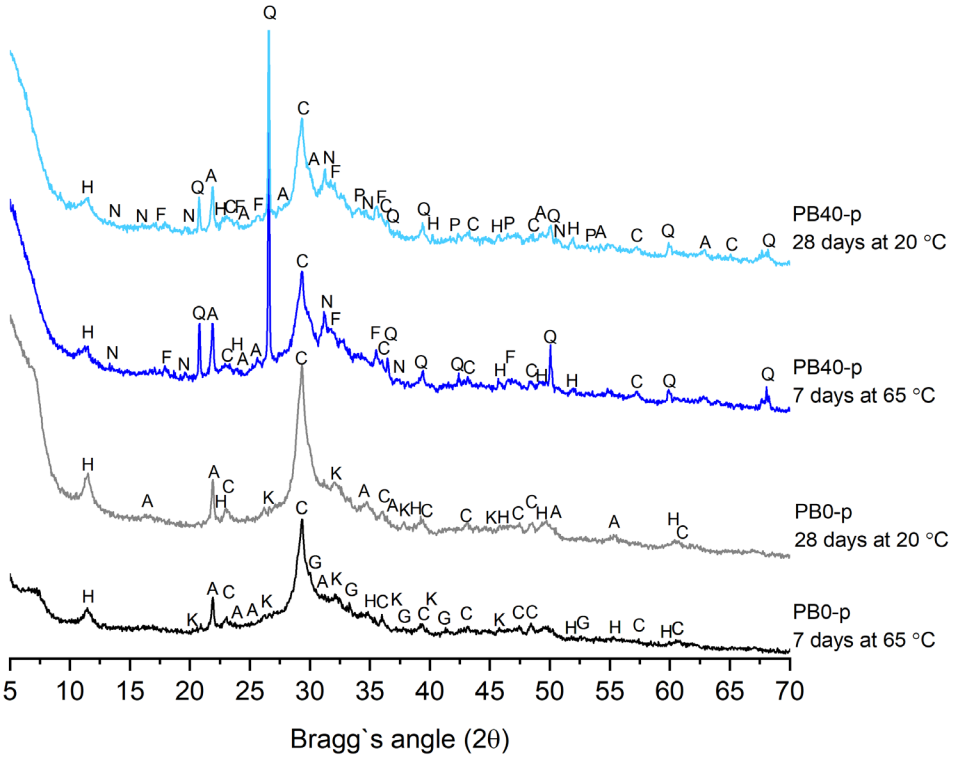

Fig. 9. XRD diffractogram of the BFS and BFS-SSA alkali-activated pastes cured for 7 days at 65ºC and for 28 days at 20ºC. C - calcite ($CaCO_3$, PDFcard 050586), A - albite ($NaAlSi_3O_8$, PDFcard 200572), H - hydrotalcite ($Mg_6Al_2CO_3(OH)_{16}.4H_2O$, PDFcard 140191), G - grossular ($Ca_3Al_2(SiO_4)_2(OH)_4$, PDFcard 310250), K - katoite ($Ca_3Al_2(SiO_4)(OH)_8$, PDFcard 380368), P - portlandite ($Ca(OH)_2$, PDFcard 040733), N - natrolite ($Na_2Al_2Si_3O_{10}.2H_2O$, PDFcard 200759) and F - forsterite (Mg_2SiO_4, PDFcard 340189).

3.4.3. Mercury intrusion porosimetry analyses.

MIP analysis was carried out with the paste (*p*) and mortar (*m*) samples containing 0 (PB0-p and PB0-m), 10 (PB10-p and PB10-m) and 40 wt.% SSA (PB40-p and PB40-m) for 28 days cured at 20ºC. The cumulative and differential intruded Hg volumes for each sample are depicted in Fig. 10. The porosity characteristics are summarised in Table 4. It was taking into account that the macropores are those with diameter higher than 0.05 µm, and the mesopores are those with diameter between 0.002 µm and 0.05 µm [45,46]. The open porosity of the paste samples was greater than those of mortars, which is the usual behaviour because of the higher amount of paste per volume unit of the analysed sample [20]. The influence of SSA was similar on both sample types. The replacement of BFS with SSA increased open porosity. While the maximum increase in open porosity was 25.6% in the mortar samples, it was 78.6% in the paste samples.

Furthermore, a substantial change in the macropore and mesopore distribution took place. When BFS was replaced with 40% SSA in the paste (PB40-p) and mortar (PB40-m), the percentage of mesopores in the samples changed from 33.1% to 77.8% and from 14.4% to 54.3%, respectively. Thus, SSA caused pore refinement in the BFS alkali-activated paste and mortar. This behaviour is clearly observed in Fig. 10, which shows a remarkable change in the curves of the cumulative and differential intruded Hg volume analysis for the mesopore region. SSA particles are more porous and present a rougher surface than BFS (Fig. 2), while the BET surface area of SSA is usually higher than BFS [23,36,47,48], which affects open porosity and the mesopores distribution observed in the MIP analysis done with the samples.

Table 4. Porosity characteristics of the pastes and mortars cured at 20ºC for 28 days.

Sample type	Identification	SSA (%)	Mesopore (%)	Macropore (%)	Mean pore diameter (µm)	Open porosity (%)
Pastes	PB0-p	0	33.1	66.9	2.38	17.8
	PB10-p	10	60.8	39.2	0.03	22.1
	PB40-p	40	77.8	22.2	0.03	31.8
Mortars	PB0-m	0	14.4	85.6	6.96	11.7
	PB10-m	10	31.6	68.4	2.85	10.4
	PB40-m	40	54.3	45.7	0.04	14.7

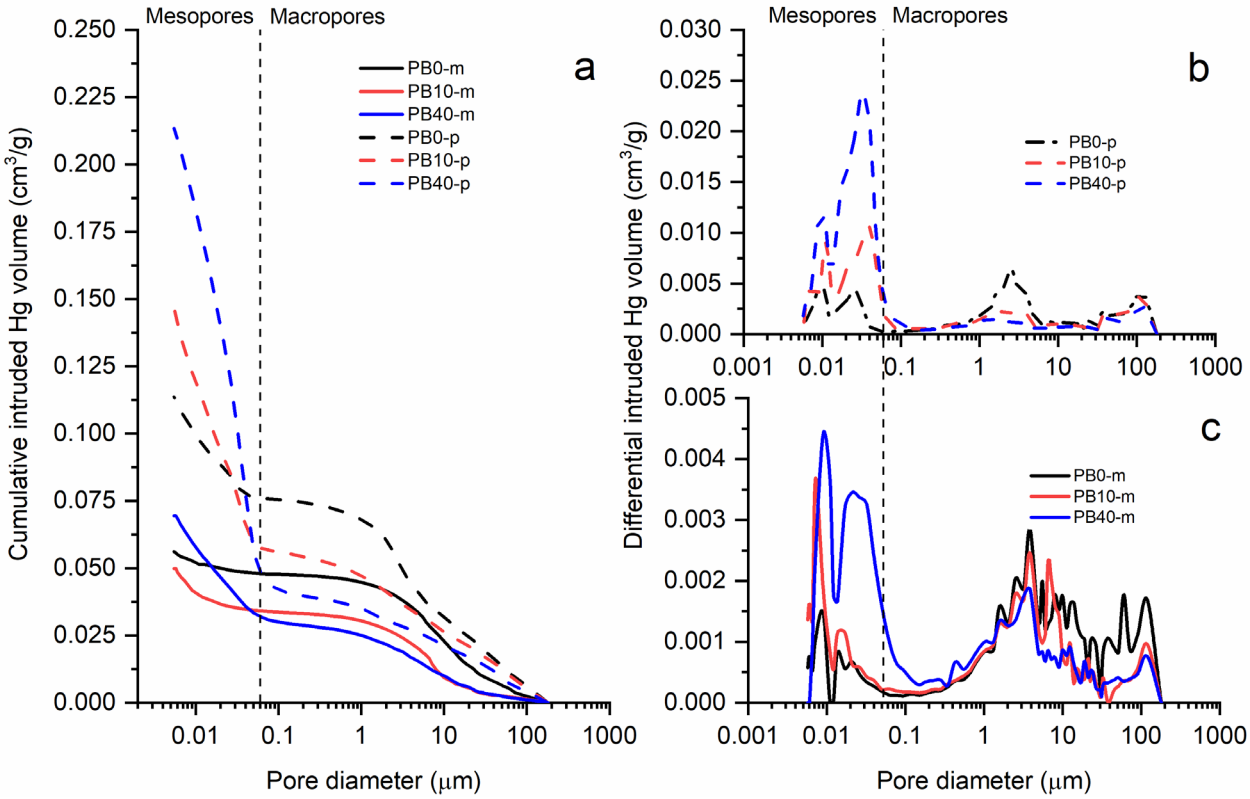

Fig. 10. Cumulative (a) and differential intruded Hg volumes of the pastes (b) and mortars (c) cured at 20ºC for 28 days.

3.4.4. Field emission scanning electron microscopy and energy dispersive X-ray spectroscopy.

FESEM-EDX analysis was carried out on the paste samples with 0% (PB0-p) and 40% SSA (PB40-p) cured at 65ºC for 7 days (Fig. 11) and at 20ºC for 28 days (Fig. 12). The EDX analyses are summarised in Table 5. In general, the samples without SSA presented a more compact microstructure than the pastes with 40% SSA. While paste PB0-p cured at 20ºC presented a more homogenous morphology, the others presented more heterogeneous morphologies, with the main gel named as C-(N)-A-S-H type in all cases (Table 5). In the selected zones of the EDX analysis, namely S1, S3, S5 and S6, a more compacted C-(N)-A-S-H gel structure (type 1) was observed [49] while a less compacted C-(N)-A-S-H gel structure (type 2) was noted in the other zones (S2 and S4) [11,50]. A notably more marked presence of the type 2 gel structure was found in pastes PB40-p, which was a less compacted structure. The propagation of cracks took place in PB40-p, which could be due to high-temperature curing and/or external forces while collecting samples for the analysis, which occurs primarily through type 2 gel. This points out that the less compacted gel could be more affected by external forces. Paste PB40-p also showed high sulphur content, which was due to the

presence of calcium sulphate (anhydrite) that was dissolved during the curing process. Sulphate anions were chemically combined or adsorbed by the cementing gel formed during the alkali activation of BFS. Moreover, unreacted particles of SSA were identified in the samples, which agrees with the XRD diffractogram of the samples containing SSA, which also showed the presence of some minerals from SSA.

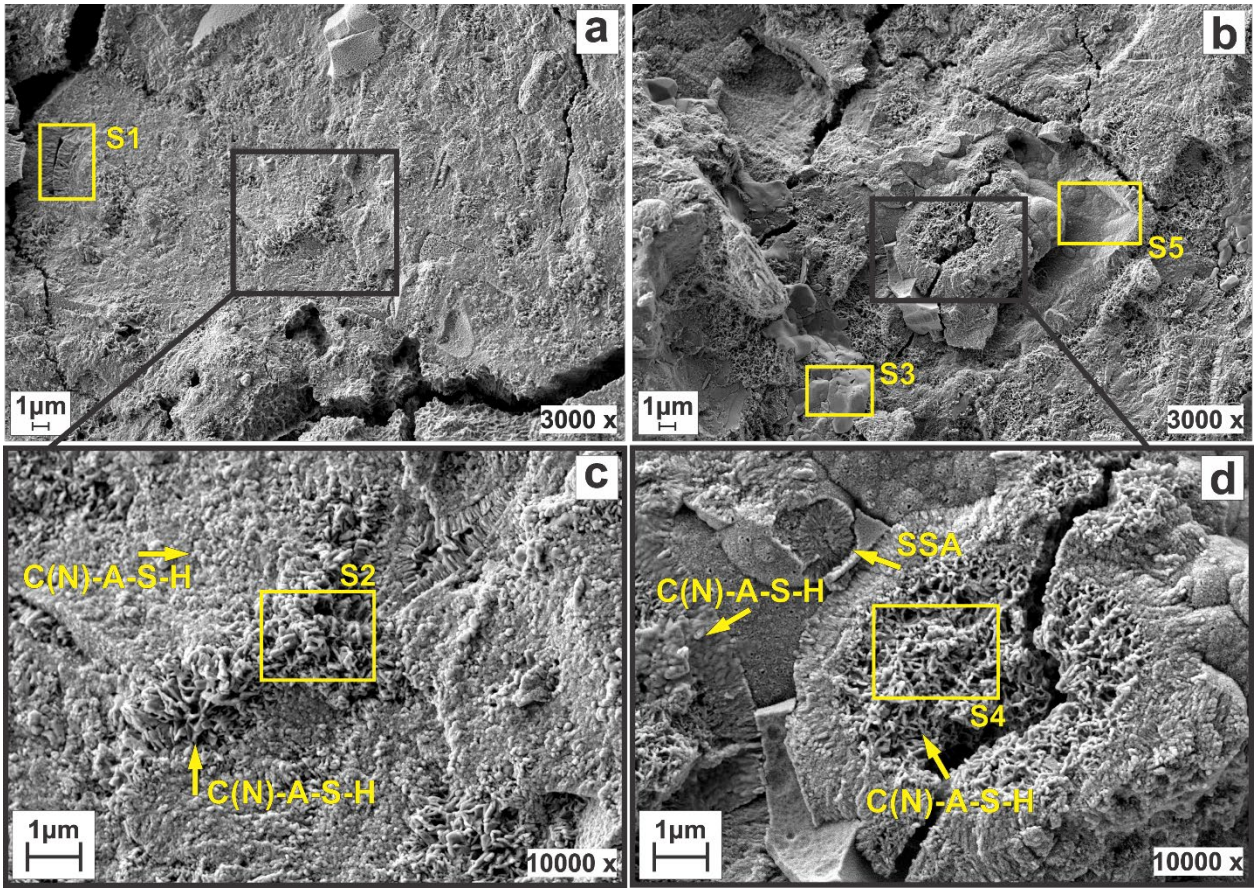

Fig. 11. SEM images of pastes PB0-p (a and c) and PB40-p (b and d) cured at 65ºC for 7 days.

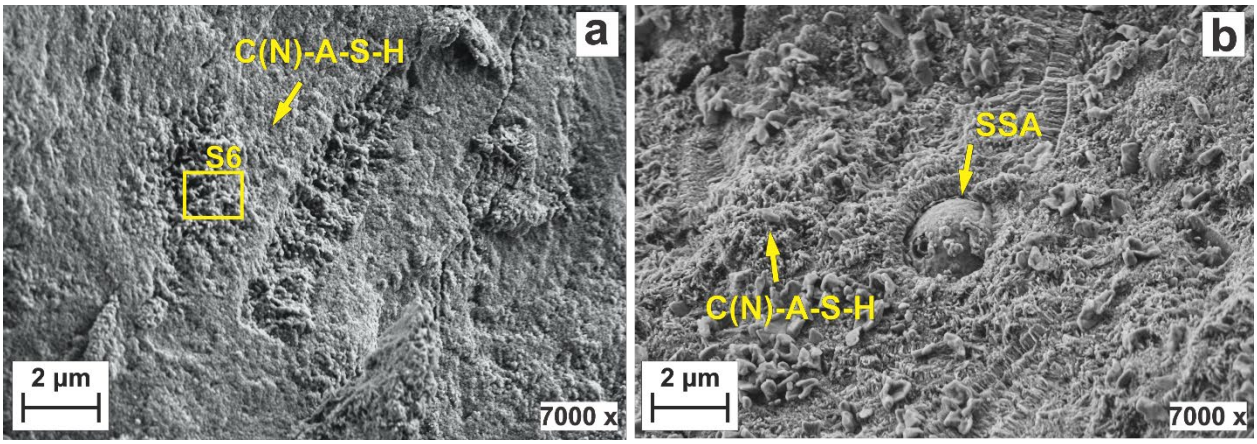

Fig. 12. SEM images of pastes PB0-p (a) and PB40-p (b) cured at 20ºC for 28 days.

Table 5. EDX analyses of C-(N)-A-S-H gel in pastes PB0-p (S1 and S2) and PB40-p (S3, S4 and S5) cured at 65ºC for 7 days (S1-S5) and cured at 20ºC for 28 days (S6).

Zone	S1	S2	S3	S4	S5	S6
Oxide (%)	More compacted C-(N)-A-S-H	Less compacted C-(N)-A-S-H	More compacted C-(N)-A-S-H	Less compacted C-(N)-A-S-H	More compacted C-(N)-A-S-H	More compacted C-(N)-A-S-H
SiO_2	41.15	40.87	21.12	37.69	34.48	36.52
CaO	31.49	30.30	25.81	28.31	27.36	37.45
Na_2O	15.51	16.60	10.34	11.15	15.42	15.91
Al_2O_3	7.25	7.38	4.34	8.49	7.92	6.87
MgO	0.75	1.74	-	2.14	2.39	1.88
K_2O	1.93	1.82	13.73	4.3	2.43	1.31
SO_3	1.93	1.28	17.03	7.92	10.01	1.54
FeO	-	-	4.14	-	-	0.43
P_2O_5	-	-	3.49	-	-	-

4. Conclusions.

This paper evaluated the compressive strength performance of binary BFS-SSA alkali-activated mortars, which the use of RHA as a silica source to prepare sodium silicate suspensions to be used as chemical activators conferred these systems more sustainability. Based on the compressive strength results and the physicochemical analysis, the following conclusions can be drawn:

(1) RHA dissolution in NaOH solution, producing sodium silicate suspensions, enhanced the compressive strength of the BFS–based alkali-activated mortars by 4.5-fold, achieving 46.9 MPa, compared to the mortar with binder 100% BFS and addition of solid (10.4 MPa).

(2) In the binary AAMs with BFS and SSA, in which RHA was added for supplying soluble silica to the medium, the compressive strength decreased with the BFS replacement by SSA. Positive values of relative compressive strength gain (CSGr) were obtained for BFS-SSA alkali-activated mortars, which means that SSA did not diminish the BFS activation.

(3) A large quantity of SSA (40 wt.%) could be incorporated into the BFS–based AAMs reaching a compressive strength, after 28 curing days at 20°C, close to 30 MPa, which is the same compressive strength level reached in similar systems reported in the literature.

(4) The microstructural characterisation analysis pointed out that the main gel formation in the binary AAMs was C-(N)-A-S-H, and SSA was a factor that increases the occurrence of a second C-(N)-A-S-H structure type, which is a less dense gel than the predominant gel type found in the paste without SSA.

(5) Due to SSA morphology, which is composed of porous and rough surface particles, the pore distribution of AAMs was refined, substantially increasing the number of mesopores, and consequently augmenting the open porosity of the binary system by 25.6% and 78.6% in the mortar and the paste samples, respectively.

Acknowledgements

This study was financed partly by the Coordenação de Aperfeiçoamento de Pessoal de Nível Superior - Brazil (CAPES) – (Finance Code 001). Thanks go to Cementval, the DACSA Group and the Pinedo Wastewater Treatment Plant for supplying some raw materials. Thanks go to the Electron Microscopy Service of the Universitat Politècnica de València.

References

[1] M.H. Samarakoon, P.G. Ranjith, T.D. Rathnaweera, M.S.A. Perera, Recent advances in alkaline cement binders: A review, J. Clean. Prod. 227 (2019) 70–87. https://doi.org/10.1016/j.jclepro.2019.04.103.

[2] J.L. Provis, A. Palomo, C. Shi, Advances in understanding alkali-activated materials, Cem. Concr. Res. 78 (2015) 110–125. https://doi.org/10.1016/j.cemconres.2015.04.013.

[3] F. Pacheco-Torgal, J. Castro-Gomes, S. Jalali, Alkali-activated binders: A review. Part 2. About materials and binders manufacture, Constr. Build. Mater. 22 (2008) 1315–1322. https://doi.org/10.1016/j.conbuildmat.2007.03.019.

[4] L.K. Turner, F.G. Collins, Carbon dioxide equivalent (CO2-e) emissions: A comparison between geopolymer and OPC cement concrete, Constr. Build. Mater. 43 (2013) 125–130. https://doi.org/10.1016/J.CONBUILDMAT.2013.01.023.

[5] C. Ng, U.J. Alengaram, L.S. Wong, K.H. Mo, M.Z. Jumaat, S. Ramesh, A review on microstructural study and compressive strength of geopolymer mortar, paste and concrete, Constr. Build. Mater. 186 (2018) 550–576. https://doi.org/10.1016/J.CONBUILDMAT.2018.07.075.

[6] F. Pacheco-Torgal, Z. Abdollahnejad, S. Miraldo, M. Kheradmand, Alkali-Activated Cement-Based Binders (AACBs) as Durable and Cost-Competitive Low-CO2 Binder Materials: Some Shortcomings That Need to be Addressed, in: Handb. Low Carbon Concr., Butterworth-Heinemann, 2017: pp. 195–216. https://doi.org/10.1016/B978-0-12-804524-4.00009-9.

[7] A. Font, L. Soriano, M.M. Tashima, J. Monzó, M.V. Borrachero, J. Payá, One-part eco-cellular concrete for the precast industry: Functional features and life cycle assessment, J. Clean. Prod. (2020) 122203. https://doi.org/10.1016/j.jclepro.2020.122203.

[8] P.O. Awoyera, A. Adesina, A. Sivakrishna, R. Gobinath, K.R. Kumar, A. Srinivas, Alkali activated binders: Challenges and opportunities, Mater. Today Proc. (2019). https://doi.org/10.1016/J.MATPR.2019.08.199.

[9] C. Ouellet-Plamondon, G. Habert, Life cycle assessment (LCA) of alkali-activated cements and concretes, 2015. https://doi.org/10.1533/9781782422884.5.663.

[10] M. Smol, J. Kulczycka, A. Henclik, K. Gorazda, Z. Wzorek, The possible use of sewage sludge ash (SSA) in the construction industry as a way towards a circular economy, J. Clean. Prod. 95 (2015) 45–54. https://doi.org/10.1016/j.jclepro.2015.02.051.

[11] M.M. Tashima, L. Reig, M.A. Santini, J.C. B Moraes, J.L. Akasaki, J. Payá, M. V. Borrachero, L. Soriano, Compressive Strength and Microstructure of Alkali-Activated Blast Furnace Slag/Sewage Sludge Ash (GGBS/SSA) Blends Cured at Room Temperature, Waste and Biomass Valorization. 8 (2017) 1441–1451. https://doi.org/10.1007/s12649-016-9659-1.

[12] S. Chakraborty, B.W. Jo, J.H. Jo, Z. Baloch, Effectiveness of sewage sludge ash combined with waste pozzolanic minerals in developing sustainable construction material: An alternative approach

547 for waste management, J. Clean. Prod. 153 (2017) 253–263.
548 https://doi.org/10.1016/j.jclepro.2017.03.059.

549 [13] Z. Chen, J.-S. Li, B.-J. Zhan, U. Sharma, C.S. Poon, Compressive strength and microstructural
550 properties of dry-mixed geopolymer pastes synthesized from GGBS and sewage sludge ash, Constr.
551 Build. Mater. 182 (2018) 597–607. https://doi.org/10.1016/j.conbuildmat.2018.06.159.

552 [14] K.T. Tong, R. Vinai, M.N. Soutsos, Use of Vietnamese rice husk ash for the production of sodium
553 silicate as the activator for alkali-activated binders, J. Clean. Prod. 201 (2018) 272–286.
554 https://doi.org/10.1016/J.JCLEPRO.2018.08.025.

555 [15] J.M. Mejía, R. Mejía de Gutiérrez, F. Puertas, Rice husk ash as a source of silica in alkali-activated
556 fly ash and granulated blast furnace slag systems, Mater. Constr. 63 (2013) 361–375.
557 https://doi.org/10.3989/mc.2013.04712.

558 [16] R. Pode, Potential applications of rice husk ash waste from rice husk biomass power plant, Renew.
559 Sustain. Energy Rev. 53 (2016) 1468–1485. https://doi.org/10.1016/j.rser.2015.09.051.

560 [17] Foreign Agricultural Service, United States Department Agriculture (USDA), (2020).
561 https://apps.fas.usda.gov/psdonline/circulars/production.pdf (accessed May 12, 2020).

562 [18] E. Kamseu, L.M. Beleuk à Moungam, M. Cannio, N. Billong, D. Chaysuwan, U.C. Melo, C.
563 Leonelli, Substitution of sodium silicate with rice husk ash-NaOH solution in metakaolin based
564 geopolymer cement concerning reduction in global warming, J. Clean. Prod. 142 (2017) 3050–3060.
565 https://doi.org/10.1016/J.JCLEPRO.2016.10.164.

566 [19] A. Mellado, C. Catalán, N. Bouzón, M. V Borrachero, J.M. Monzó, J. Payá, Carbon footprint of
567 geopolymeric mortar: Study of the contribution of the alkaline activating solution and assessment of
568 an alternative route, RSC Adv. 4 (2014) 23846–23852. https://doi.org/10.1039/c4ra03375b.

569 [20] A. Font, L. Soriano, S.M. de Moraes Pinheiro, M.M. Tashima, J. Monzó, M.V. Borrachero, J. Payá,
570 Design and properties of 100% waste-based ternary alkali-activated mortars: Blast furnace slag,
571 olive-stone biomass ash and rice husk ash, J. Clean. Prod. 243 (2020) 118568.
572 https://doi.org/10.1016/j.jclepro.2019.118568.

573 [21] N. Bouzón, J. Payá, M. V. Borrachero, L. Soriano, M.M. Tashima, J. Monzó, Refluxed rice husk
574 ash/NaOH suspension for preparing alkali activated binders, Mater. Lett. 115 (2014) 72–74.
575 https://doi.org/10.1016/j.matlet.2013.10.001.

576 [22] J.C.B.C.B. Moraes, A. Font, L. Soriano, J.L.L. Akasaki, M.M.M. Tashima, J. Monzó, M.V. V.

577 Borrachero, J. Payá, New use of sugar cane straw ash in alkali-activated materials: A silica source
578 for the preparation of the alkaline activator, Constr. Build. Mater. 171 (2018) 611–621.
579 https://doi.org/10.1016/j.conbuildmat.2018.03.230.

580 [23] J. Payá, J. Monzó, M. V. Borrachero, A. Mellado, L.M. Ordoñez, Determination of amorphous silica
581 in rice husk ash by a rapid analytical method, Cem. Concr. Res. 31 (2001) 227–231.
582 https://doi.org/10.1016/S0008-8846(00)00466-X.

583 [24] UNE-EN 196-1:2018, Methods of Testing Cement – Part 1: Determination of Strength, (2018).
584 https://www.en-standard.eu/une-en-196-1-2018-methods-of-testing-cement-part-1-determination-
585 of-strength/.

586 [25] J.M. Paris, J.G. Roessler, C.C. Ferraro, H.D. DeFord, T.G. Townsend, A review of waste products
587 utilized as supplements to Portland cement in concrete, J. Clean. Prod. 121 (2015) 1–18.
588 https://doi.org/10.1016/j.jclepro.2016.02.013.

589 [26] A. Pereira, J.L. Akasaki, J.L.P. Melges, M.M. Tashima, L. Soriano, M. V. Borrachero, J. Monzó, J.
590 Payá, Mechanical and durability properties of alkali-activated mortar based on sugarcane bagasse
591 ash and blast furnace slag, Ceram. Int. 41 (2015) 13012–13024.
592 https://doi.org/10.1016/j.ceramint.2015.07.001.

593 [27] Y. Jin, W. Feng, D. Zheng, Z. Dong, H. Cui, M. Li, G. Sang, W. Tang, Study on the interaction
594 mechanism between slags and alkali silicate activators: A hydration kinetics approach, Constr.
595 Build. Mater. 250 (2020) 118900. https://doi.org/10.1016/J.CONBUILDMAT.2020.118900.

596 [28] J. Monzó, J. Payá, M. V Borrachero, I. Girbés, Reuse of sewage sludge ashes (SSA) in cement
597 mixtures: the effect of SSA on the workability of cement mortars., Waste Manag. 23 (2003) 373–
598 81. https://doi.org/10.1016/S0956-053X(03)00034-5.

599 [29] F. Puertas, C. Varga, M.M. Alonso, Rheology of alkali-activated slag pastes. Effect of the nature
600 and concentration of the activating solution, Cem. Concr. Compos. 53 (2014) 279–288.
601 https://doi.org/10.1016/j.cemconcomp.2014.07.012.

602 [30] J. Monzó, J. Payá, M.. Borrachero, E. Peris-Mora, Mechanical behavior of mortars containing
603 sewage sludge ash (SSA) and Portland cements with different tricalcium aluminate content, Cem.
604 Concr. Res. 29 (1999) 87–94. https://doi.org/10.1016/S0008-8846(98)00177-X.

605 [31] M. Tashima, L. Soriano, J. Monzó, M. Borrachero, J. Akasaki, J. Payá, New method to assess the
606 pozzolanic reactivity of mineral admixtures by means of pH and electrical conductivity

607 measurements in lime: pozzolan suspensions, Mater. Construcción; Vol 64, No 316. 64 (2014) 1–
608 12. https://doi.org/10.3989/mc.2014.00914.

609 [32] M.N.N. Khan, M. Jamil, M.R. Karim, M.F.M. Zain, A.B.M.A. Kaish, Filler effect of pozzolanic
610 materials on the strength and microstructure development of mortar, KSCE J. Civ. Eng. 21 (2017)
611 274–284. https://doi.org/10.1007/s12205-016-0737-5.

612 [33] C.J. Lynn, R.K. Dhir, G.S. Ghataora, R.P. West, Sewage sludge ash characteristics and potential for
613 use in concrete, Constr. Build. Mater. 98 (2015) 767–779.
614 https://doi.org/10.1016/j.conbuildmat.2015.08.122.

615 [34] G. Habert, J.B. D'Espinose De Lacaillerie, N. Roussel, An environmental evaluation of geopolymer
616 based concrete production: Reviewing current research trends, J. Clean. Prod. 19 (2011) 1229–1238.
617 https://doi.org/10.1016/j.jclepro.2011.03.012.

618 [35] I. Garcia-Lodeiro, A. Fernández-Jiménez, An overview of the chemistry of alkali-activated cement-
619 based binders, Handb. Alkali-Activated Cem. Mortars Concr. (2015) 19–47.
620 https://doi.org/10.1533/9781782422884.1.19.

621 [36] J. Xing, Y. Zhao, J. Qiu, X. Sun, Microstructural and mechanical properties of alkali activated
622 materials from two types of blast furnace slags, Materials (Basel). 12 (2019).
623 https://doi.org/10.3390/ma12132089.

624 [37] S.J. Bae, S. Park, H.K. Lee, Role of Al in the crystal growth of alkali-activated fly ash and slag under
625 a hydrothermal condition, Constr. Build. Mater. 239 (2020) 117842.
626 https://doi.org/10.1016/j.conbuildmat.2019.117842.

627 [38] O. Burciaga-Díaz, L.Y. Gómez-Zamorano, J.I. Escalante-García, Influence of the long term curing
628 temperature on the hydration of alkaline binders of blast furnace slag-metakaolin, Constr. Build.
629 Mater. 113 (2016) 917–926. https://doi.org/10.1016/j.conbuildmat.2016.03.111.

630 [39] J. Yang, Y. Shi, X. Yang, M. Liang, Y. Li, Y. Li, N. Ye, Durability of autoclaved construction
631 materials of sewage sludge–cement–fly ash–furnace slag, Constr. Build. Mater. 48 (2013) 398–405.
632 https://doi.org/10.1016/j.conbuildmat.2013.07.018.

633 [40] C.S. Thunuguntla, T.D. Gunneswara Rao, Appraisal on Strength Characteristics of Alkali-Activated
634 GGBFS with Low Concentrations of Sodium Hydroxide, Iran. J. Sci. Technol. - Trans. Civ. Eng. 42
635 (2018) 231–243. https://doi.org/10.1007/s40996-018-0113-4.

636 [41] P. Rożek, M. Król, W. Mozgawa, Geopolymer-zeolite composites: A review, J. Clean. Prod. 230

637 (2019) 557–579. https://doi.org/10.1016/J.JCLEPRO.2019.05.152.

638 [42] J. Davidovits, Application of Ca-based geopolymer with blast furnace slag , a review, Proceeding
639 Second Int. Slag Valoris. Symp. (2011) 33–49.

640 [43] F. Agrela, M. Cabrera, M.M. Morales, M. Zamorano, M. Alshaaer, Biomass fly ash and biomass
641 bottom ash, in: New Trends Eco-Efficient Recycl. Concr., Elsevier, 2018: pp. 23–58.
642 https://doi.org/10.1016/B978-0-08-102480-5.00002-6.

643 [44] S.A. Bernal, E.D. Rodríguez, R.M. De Gutiérrez, J.L. Provis, Performance at high temperature of
644 alkali-activated slag pastes produced with silica fume and rice husk ash based activators, Mater.
645 Constr. 65 (2015) 49. https://doi.org/10.3989/mc.2015.03114.

646 [45] F.G.M. Aredes, T.M.B. Campos, J.P.B. Machado, K.K. Sakane, G.P. Thim, D.D. Brunelli, Effect of
647 cure temperature on the formation of metakaolinite-based geopolymer, Ceram. Int. 41 (2015) 7302–
648 7311. https://doi.org/10.1016/j.ceramint.2015.02.022.

649 [46] J. Wang, P. Du, Z. Zhou, D. Xu, N. Xie, X. Cheng, Effect of nano-silica on hydration, microstructure
650 of alkali-activated slag, Constr. Build. Mater. 220 (2019) 110–118.
651 https://doi.org/10.1016/j.conbuildmat.2019.05.158.

652 [47] M. Cyr, M. Coutand, P. Clastres, Technological and environmental behavior of sewage sludge ash
653 (SSA) in cement-based materials, Cem. Concr. Res. 37 (2007) 1278–1289.
654 https://doi.org/10.1016/j.cemconres.2007.04.003.

655 [48] Y.J. Patel, N. Shah, Enhancement of the properties of Ground Granulated Blast Furnace Slag based
656 Self Compacting Geopolymer Concrete by incorporating Rice Husk Ash, Constr. Build. Mater. 171
657 (2018) 654–662. https://doi.org/10.1016/J.CONBUILDMAT.2018.03.166.

658 [49] J.C.B. Moraes, M.M. Tashima, J.L. Akasaki, J.L.P. Melges, J. Monzó, M.V. Borrachero, L. Soriano,
659 J. Payá, Effect of sugar cane straw ash (SCSA) as solid precursor and the alkaline activator
660 composition on alkali-activated binders based on blast furnace slag (BFS), Constr. Build. Mater. 144
661 (2017) 214–224. https://doi.org/10.1016/J.CONBUILDMAT.2017.03.166.

662 [50] D. Zhao, Y. Gao, S. Nie, Z. Liu, F. Wang, P. Liu, S. Hu, Self-assembly of honeycomb-like calcium-
663 aluminum-silicate-hydrate (C-A-S-H) on ceramsite sand and its application in photocatalysis, Chem.
664 Eng. J. 344 (2018) 583–593. https://doi.org/10.1016/J.CEJ.2018.03.074.